Overcoming the Absorption Bottleneck for Solid-State Infrared-to-Visible Upconversion

Pournima Narayanan[1,2], Manchen Hu[1], Arynn O. Gallegos[1], Linda Pucurimay[1,3], Qi Zhou[1], Emma Belliveau[1], Ghada H. Ahmed[1], Sebastian Fernández[1], William Michaels[1], Natalia Murrietta[1], Vongaishe E. Mutatu[1], Demeng Feng[4], Rabeeya Hamid[4], Kyra M. K. Yap[5], Tracy H. Schloemer[1], Thomas F. Jaramillo[5], Mikhail A. Kats[4], Dan Congreve[1]*

[1] Department of Electrical Engineering, Stanford University, Stanford, CA 94305, USA

[2] Department of Chemistry, Stanford University, Stanford, CA 94305, USA

[3] Department of Material Science Engineering, Stanford University, Stanford, CA 94305, USA

[4] Department of Electrical and Computer Engineering, University of Wisconsin - Madison, Madison, WI 53706, USA

[5] Department of Chemical Engineering, Stanford University, Stanford, CA 94305, USA

*Corresponding author email: Congreve@stanford.edu

Abstract:

Upconversion (UC) of low-energy photons to higher-energy photons has enabled exciting advances in applications such as 3D printing, bioimaging, and more. In particular, UC of near infrared photons into visible photons has been identified as a process which can enhance photovoltaic, night vision, and anti-counterfeiting technologies. Triplet-triplet annihilation UC is particularly attractive for these applications due to its low upconversion thresholds and broadband, tunable absorption. However, current state-of-the-art near-infrared-to-visible triplet-triplet annihilation solid-state UC devices made of PbS quantum dots and rubrene are limited by (1) low absorption of near infrared photons, (2) low energy transfer rates, and (3) highly parasitic back transfer processes, leading to low external quantum efficiencies unsuitable for wide application. Here, we propose a device architecture that allows for strongly absorbing PbS films with improved efficiencies. We use 5-tetracene carboxylic acid as an interlayer to improve Dexter energy transfer to rubrene and alleviate parasitic back transfer leading to an improvement by a factor of 5 compared to control devices. Finally, we demonstrate that these devices allow for visible upconversion anti-counterfeiting with an incoherent light source at modest intensities, highlighting their potential for UC-facilitated technologies.

Keywords: Triplet-Triplet Annihilation; Upconversion; NIR; PbS Quantum Dots; Anti-counterfeiting; Tetracene-5-carboxylic acid

Main:

Photon upconversion (UC), the process of converting low energy photons into higher energy photons, holds tremendous potential for various applications including photovoltaics,[1–5] night vision,[6] photocatalysis,[7–10] bioimaging,[11–17] anti-counterfeiting,[18–20] additive manufacturing,[21–24] and more.[25–28] The anti-Stokes shift achieved by short-wave- and near-infrared-to-visible UC is instrumental to address the bandgap limitations of silicon[2,3,6,29] and to exploit the positioning of key transparency windows in biological systems.[30–33] By absorbing sub-bandgap photons in the near infrared (NIR) region, UC-assisted photovoltaics have been proposed to achieve higher efficiencies beyond single-junction solar cells.[2,3,5] Additionally, the difficulty in replicating NIR-to-visible anti-Stokes shifts presents an opportunity to employ UC for anti-counterfeiting applications.[18–20]

There have been several reported mechanisms to achieve visible emission from NIR excitation, including excited-state absorption,[27,34] energy-transfer UC,[27,34] photon avalanching,[27,34,35] collective energy pooling,[36] and triplet-triplet annihilation upconversion (TTA-UC).[27,37] Various f-block elements have been deployed in nanocrystals and solids to achieve tunable, sharp, and significantly anti-Stokes shifted emission by creating ultraviolet or visible photons from NIR photons.[27] Despite the large anti-Stokes shift achieved by these systems *via* f—f transitions, they are often limited in applicability due to their need for high intensities of coherent light and narrow absorption bands.[25, 27, 28] UC *via* TTA shows particular promise for applications because it can occur relatively efficiently under lower intensity irradiation from incoherent and broadband sources of light.[25,27,28]

In the overall TTA-UC process, two low-energy photons are absorbed (by the sensitizer) and converted into one higher-energy photon (emitted by the annihilator). The mechanism of TTA-UC relies on two species: the sensitizer and the annihilator (see Figure 1a). The annihilator is an organic semiconductor (often an acene) with energetics such that two triplet-excited annihilator molecules can interact *via* TTA to generate one singlet-excited and one ground-state annihilator molecule. The singlet-excited annihilator molecule can then relax to the ground state by emitting a high energy photon *via* photoluminescence (PL). As shown in Figure 1a, sensitizers are necessary to create triplet-excited annihilator molecules, as triplet states in organic semiconductors are typically optically inaccessible. Sensitizer species absorb light (Abs) to create an excited state (typically a singlet), which can undergo intersystem crossing (ISC) to generate a triplet which can transfer its energy to an annihilator *via* Dexter energy transfer (ET). There are various families of sensitizers for TTA including semiconducting quantum dots (QDs),[38–40] thermally activated delayed fluorescence molecules,[41,42] heavy metal porphyrin complexes,[37,43] and non-fullerene acceptors.[44,45]

Commercial realization of solid-state NIR-to-visible UC demands that this conversion process be highly efficient. Zhou et al. have summarized essential metrics to measure the efficiency of UC systems.[46] Here, we use the external quantum efficiency (EQE) as a performance metric due to its relevance to applications like photovoltaics, night vision, and anti-counterfeiting. EQE is defined as the number of upconverted photons generated by 100 incident low-energy photons. To follow the norms adopted by the field, all EQEs in this article will be reported with a maximum possible 50% (due to the two-photons-to-one-photon nature of TTA-UC).[46]

Arguably the most well-studied annihilator for NIR-to-visible UC to date is rubrene (see Figure 1c), a tetracene derivative.[47] DBP, an organic semiconductor (see Figure 1c), is often doped into rubrene films to improve the resulting photoluminescence quantum yield (PLQY) by acting as a singlet sink to prevent triplet separation.[48,49] Rubrene has been reported to be sensitized by a wide range of materials, including organic semiconductors (Y6, ITIC-Cl),[44,45,50] semiconducting QDs (PbS, PbSe),[39,40,51–53] 2D transition metal dichalcogenides,[54,55] and heavy metal complexes (PdPc, PtTPTNP, osmium complexes, and more).[5,56–59] Despite promising performance from different sensitizers, most NIR-to-visible systems are limited to excitation wavelengths below ~1000 nm.

PbS QDs are highly appealing sensitizers due to their broad and tunable absorption spectra which can span the NIR region (650-2000 nm) through well-established synthetic control of their diameter.[60] The PbS-rubrene/DBP system has shown visible UC emission from excitations up to 1100 nm.[39] Successful solid-state NIR-to-visible UC systems employing PbS quantum dots as the sensitizer and rubrene as the annihilator (see Figure 1a, b) were reported in 2016 with EQEs of under 0.0003%.[39] Since this initial demonstration, there have been reports which have improved the efficiencies of this system using mirrors[61] and cavities,[62] with champion EQEs of 0.06% reported by M. Wu, et al. in 2021 *via* the use of a Fabry-Perot cavity. Still, using cavities severely limits the broadband absorption, and therefore deters the application of this structure to applications such as photovoltaics, night vision, and anti-counterfeiting. Consequently, an approach at the device engineering level is urgently needed to enhance the absorption and efficiency of these devices.

To improve the EQEs of UC devices towards realizing their potential, we pursued improvements to the various components contributing to the EQE. The EQE of the TTA-UC process can be broken down as the product of absorption and internal quantum efficiency (IQE). The IQE can be further broken down as the product of the efficiencies of energy transfer (φ_{ET}), TTA (φ_{TTA}), and photoluminescence (φ_{PL}) (see Equation 1).[25,46] As shown in Figure 1d, efficient energy transfer (ET) from PbS QDs to rubrene is essential to maximize the triplet density in rubrene. This energy transfer in the forward direction (PbS QDs → rubrene) is of the Dexter type, i.e., the energy transfer rate is exponentially dependent on the distance between the donor (PbS QDs) and acceptor (rubrene).[40,52,53,63–67] The insulating organic ligand shell (typically, oleic acid) adhered to the PbS QDs is known to hinder the ET efficiency due to increased spatial distance between the donor and acceptor.[40,68] This issue has been commonly overcome through the use of shorter ligands or extractor/mediator ligands on the QDs.[40,64,69–73]

$$\mathrm{EQE} = \varphi_A \times \mathrm{IQE} = \varphi_A \times \varphi_{ET} \times \varphi_{TTA} \times (1-\varphi_{BT}) \times \varphi_{PL} \qquad \text{Equation 1}$$

However, another major loss mechanism has been identified as a source of low efficiencies for solid-state UC beyond ET from the PbS QD to rubrene. [52,53,65–68,74–76] This loss mechanism involves parasitic energy back transfer (BT) from the rubrene singlet to the PbS QDs, as shown in Figure 1d. This BT process (rubrene singlet → PbS QDs) is a Förster resonance energy transfer (FRET) process which is exacerbated by high acceptor (PbS QD) concentrations leading to a severe drop in IQE for thicker PbS films deposited from solutions with concentrations beyond 5-10 mg/mL.[52,53,65–68,74–76] Therefore, traditional PbS QD/rubrene devices report 1-2 monolayer thin PbS films with low absorptions on the order of 0.1-0.5% (excluding examples employing cavities).[39,68,77] Thus far, this low absorption has presented a bottleneck to high EQEs in QD-based solid-state TTA-UC.

The aforementioned forward (ET) and backward (BT) energy transfer processes present a paradoxical simultaneous need for proximity and distance between the sensitizer and annihilator to maximize device EQEs. To address this challenge, we propose the introduction of an intermediate triplet-diffusing, FRET-blocking organic layer between the PbS QDs and rubrene layers (see Figure 1e). We hypothesize that the introduction of some optimal thickness of an organic semiconductor would improve EQEs by reducing the BT process. This ideal interlayer would possess a triplet energy level between that of rubrene (T_1 = 1.14 eV)[78] and the PbS QD bandgap (~1.2 eV) while possessing a singlet energy level higher than that of rubrene (S_1 = 2.25 eV).[78] As shown in Figure 1e, this proposed device architecture prevents the parasitic BT by acting as an uphill energetic barrier while maintaining the triplet energy flow to the rubrene through downhill energy transfer processes (ET1, ET2).[65,67,74,75]

Here, we report the use of 5-tetracene carboxylic acid (TCA, S_1 = 2.4 eV, T_1 = ~1.3 eV, see Figure 1e)[79] as an interlayer to improve NIR-to-visible solid-state UC. In addition to improvements in BT alleviation (i.e., reduction in φ_{BT}), we observe improvements in triplet extraction ($\varphi_{ET1/ET}$) efficiencies from PbS. We report significant improvements in EQE, particularly for thicker PbS films, and systematically identify the cause of the improvement in EQE. Finally, we demonstrate the application of this novel device architecture in anti-counterfeiting by depositing a patterned TCA interlayer to create intricate images under diffuse NIR irradiation.

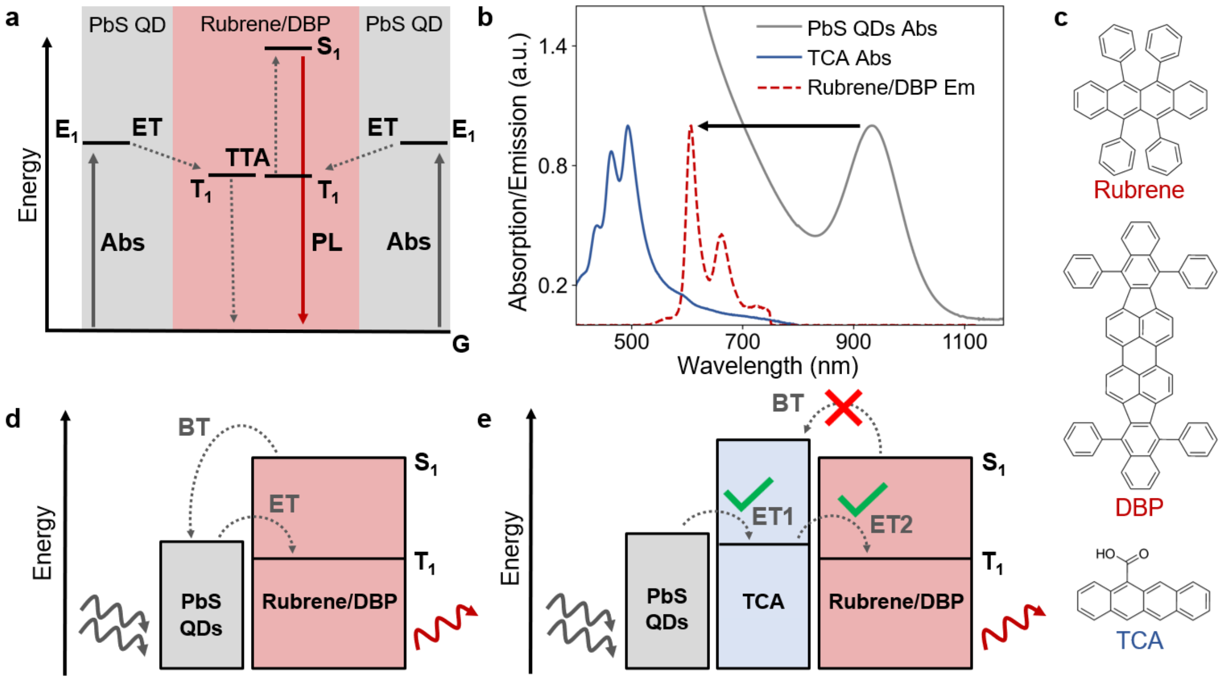

Figure 1: **(a)** Schematic energy diagram showing the mechanism of triplet-triplet annihilation upconversion (TTA-UC). PbS QDs absorb (Abs) incident NIR light to sensitize rubrene *via* energy transfer (ET). Two triplet-excited rubrene molecules undergo triplet-triplet annihilation (TTA) to emit a visible photon (PL). **(b)** Emission spectrum of rubrene/DBP (1 vol% doping of DBP in rubrene) (dashed, red) and absorption spectra of PbS (gray) and TCA (blue). Arrow highlights the anti-Stokes shift achieved by this system. **(c)** Molecular structures of rubrene (S_1 = 2.25, T_1 = 1.14 eV), DBP, and TCA (5-tetracene carboxylic acid, S_1 = 2.4 eV, T_1 = ~1.3 eV). **(d)** Energy diagram of the traditional PbS-rubrene/DBP UC device architecture with gray, dotted arrows highlighting the energy transfer processes. **(e)** Energy diagram of our proposed device architecture with an interlayer between rubrene and PbS QDs such that ET in the forward direction is maintained and parasitic back transfer (BT) is reduced to improve UC performance.

Results:

External Quantum Efficiency Measurements:

We fabricated the traditional NIR-to-visible UC devices (see Figure 1d) by spin coating PbS QDs from toluene on cleaned glass substrates followed by annealing at 70 °C and thermal co-evaporation of approximately 64 nm (optimized for our device stack) of 1 vol% DBP in rubrene on top. For our novel device architecture (Figure 1e), TCA was spin-coated on top of the PbS QD film before annealing and thermal co-evaporation of approximately 64 nm of rubrene/DBP. All UC devices were encapsulated with glass slides using UV-curing epoxy glue to prevent oxygen ingress. These devices were excited using an 808 nm laser to observe UC from rubrene/DBP (550-750 nm emission) through a 750 nm short-pass filter (see UC emission spectrum of rubrene/DBP in Figure 1b). See the Methods section for further details on the UC photoluminescence measurements.

To study the UC performance, we measured the EQEs using the EQE calculation method reported by Izawa, et al.[44] and Hu, et al.[50] (see the Methods section for more details). We varied the thickness of the TCA by spin coating solutions with varying concentrations of TCA in acetonitrile (1-6 mM, see Figure SI 8 for TCA optimization). Additionally, we tuned the PbS thickness by varying the PbS solution concentration between 5 and 50 mg/mL to deposit films which absorb between 0.3 and 6.2% of the incident 808 nm laser (see SI Note 1 and 2 for percent absorption calculations). As shown by the orange trace in Figure 2a, there was a steady decline in EQE for the control devices with increasing PbS thickness (no TCA). While thicker PbS films are expected to absorb more NIR photons, they also suffer from more parasitic BT of singlet excitons from rubrene/DBP. Additionally, the energy transfer between QDs is limited due to the insulating shell created by the oleic acid ligands. This shell also limits the energy transfer from PbS to rubrene/DBP. So far, this decline in EQE with increasing PbS thickness has presented a crucial bottleneck to unlocking higher EQEs in this system.

Upon introduction of the optimal 3 mM TCA between PbS and rubrene/DBP, we observe a sharp EQE increase at all PbS film thicknesses. Excitingly, we achieved the highest EQE in our experiments for the thickest PbS films (50 mg/mL) allowing an absorption up to 6.2% of incident 808 nm light without the use of cavities or mirrors (Figure 2a). We hypothesize that the massive improvements in EQE originate from (1) an improvement in energy transfer from PbS QDs, and (2) alleviated BT from rubrene/DBP to PbS QDs (*vide infra)*. Based on atomic force microscopy (AFM) measurements, we isolated the thickness of 3 mM TCA to be approximately 10 nm (see SI Figure 3 and 4). This thickness of 3 mM TCA and the higher singlet energy level of TCA support our hypothesis that TCA alleviates FRET-based energy BT from rubrene/DBP to PbS QDs (φ_{BT}) (see Figure 1e). Additionally, the triplet level of TCA lies near the PbS bandgap and above the rubrene triplet, allowing and facilitating the energy transfer in the forward direction.

Interestingly, upon increasing the thickness of TCA to approximately 19 nm by spinning a higher concentration of 6 mM TCA, we observed a decline in EQE relative to the optimal 3 mM TCA. While the thicker TCA layer would prevent back-FRET energy transfer further, the triplets within the TCA now face non-radiative recombination pathways before reaching the TCA-rubrene/DBP interface (i.e., φ_{BT} decreases, φ_{ET2} also faces a drop with thicker TCA films).

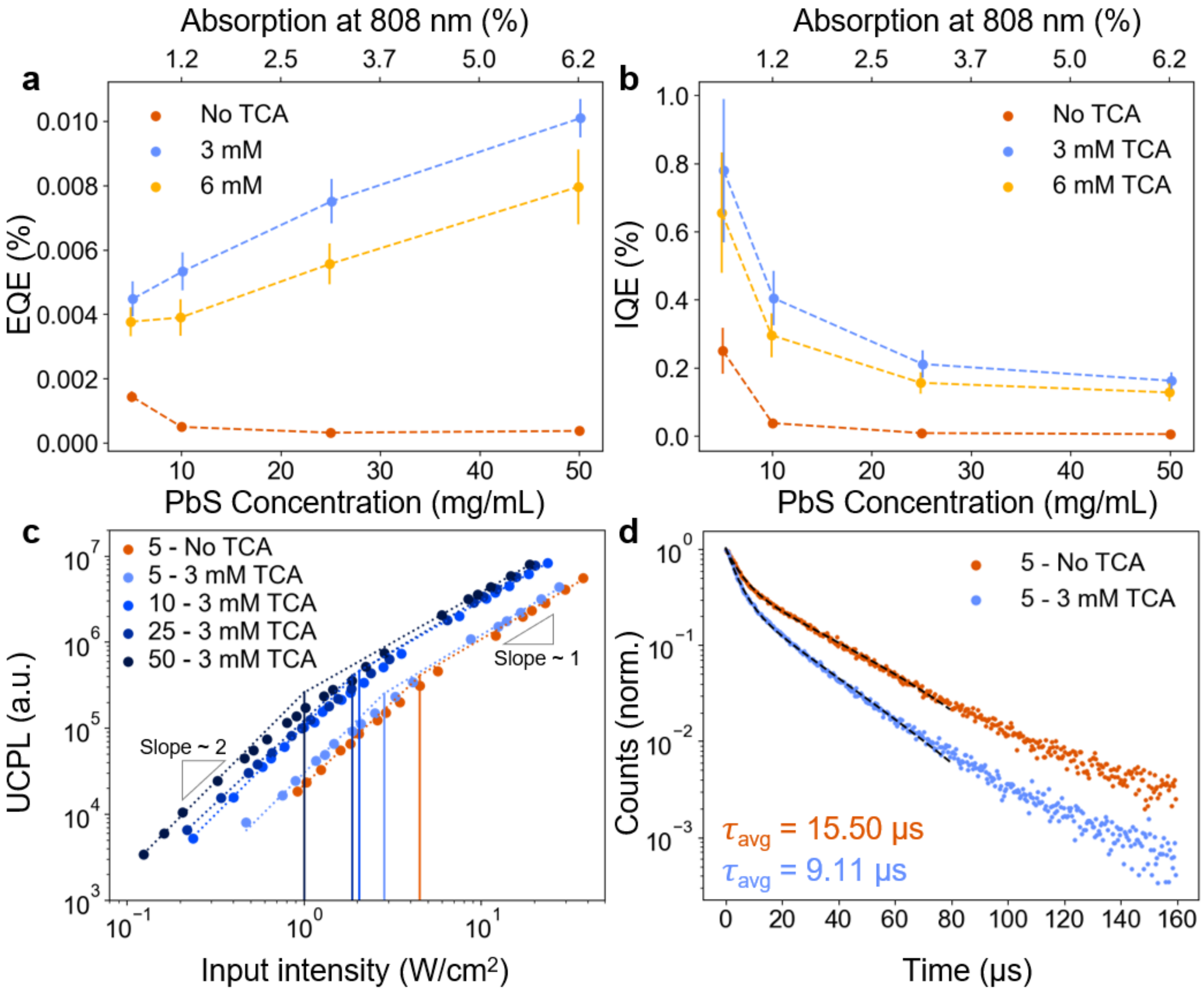

Figure 2: **(a)** Absolute external quantum efficiencies (EQEs) and **(b)** internal quantum efficiencies (IQEs) of UC devices with varying TCA (3 mM and 6 mM), PbS concentrations (5, 10, 25, 50 mg/mL), and percent absorption at 808 nm. Control devices without TCA are shown in orange. **Note:** dashed lines are used only to highlight the trends with varying PbS concentrations. **(c)** UC power dependence used to calculate the UC threshold intensities of 5 mg/mL PbS QDs devices with and without TCA (3 mM). Threshold intensities (bottom right) and slopes of linear and quadratic regimes are reported in Figure SI 9 and SI Table 1. **(d)** Time-resolved UC photoluminescence (TRUCPL) decay curves of 5 mg/mL PbS QDs devices with and without TCA (3 mM). Decay curves for 10, 25, and 50 mg/mL PbS with 3 mM TCA are reported in Figure SI 10 and SI Table 2.

Internal Quantum Efficiency Measurements:

Since EQE is defined as the product of percent absorption and IQE (see Equation 2), the IQE can be calculated as the EQE divided by the percent absorption. When we normalized the EQEs with percent absorption to obtain IQEs, we observed that the IQE remains highest for 5 mg/mL PbS QDs (see Figure 2b) with or without TCA. At increasing PbS film thicknesses, the IQE drops. However, for devices with thicker PbS films, the IQE improvement achieved by the incorporation of TCA is extremely high (27× improvement for 50 mg/mL PbS from (0.006 ± 0.001)% to (0.163 ± 0.026)%). For applications like photovoltaics and night vision, high absorption and high IQE are both required, yet have thus far a rise in absorption has been related to a significant drop in IQE of UC devices. This work presents a large stride towards the goal of simultaneous maximization of IQE *and* absorption.

$$\mathrm{EQE} = \varphi_A \times \mathrm{IQE} = \varphi_A \times \varphi_{ET1} \times \varphi_{ET2} \times (1\text{-}\varphi_{BT}) \times \varphi_{TTA} \times \varphi_{PL} \qquad \text{Equation 2}$$

TRUCPL and UC Threshold Measurements:

To probe the source of improvements in EQE and IQE, we performed time-resolved upconversion photoluminescence (TRUCPL) and UC threshold measurements. We performed these measurements on 5 mg/mL PbS films with and without 3 mM TCA. To probe the effect of increasing PbS film thicknesses, we also performed these measurements on 10, 25, and 50 mg/mL PbS films with 3 mM TCA. We note that the control devices (without TCA) for thicker PbS films lacked sufficient UC signal to perform TRUCPL and threshold measurements.

The TRUCPL decays were fitted using the biexponential function in Equation 3 (see Figure 2d and SI Table 2). We observed a decrease in the average lifetime of the devices with 3 mM TCA (9.11 μs) compared to control devices without TCA (15.50 μs). Additionally, we observed a ~50% decrease in the UC threshold for devices with TCA (decreasing from 4.50 W/cm^2 to 2.82 W/cm^2) (see Figure 2c). TCA-enhanced UC devices with increasing PbS thicknesses showed a consistent drop in threshold intensity going from 2.82 W/cm^2 for 5 mg/mL PbS to ~1 W/cm^2 for 50 mg/mL PbS (see Figure SI 9 and SI Table 1)

$$y = A_1 \exp\left(\frac{-\tau}{\tau_1}\right) + A_2 \exp\left(\frac{-\tau}{\tau_2}\right) \qquad \text{Equation 3}$$

Both TRUCPL and threshold intensity measurements signify an increased concentration of triplets in the rubrene/DBP layer upon the introduction of TCA. Since TCA possesses a carboxylic acid group which has a strong affinity to bind to the surface of PbS QDs, we hypothesize that it behaves as an extractor/mediator ligand to aid in energy transfer to the annihilator in addition to reducing back ttransfer.[51,70,73] Additionally, since triplet excitons in organic semiconductors are long-lived, the extraction of excitons by semiconducting ligands helps overcome the radiative and non-radiative losses that hinder the triplet transfer from PbS QDs without extractor ligands.[51,70,73] Here, we postulate that the binding of TCA to PbS QDs increases the exciton extraction efficiency (φ_{ET1}). Still, since the device improvements could originate from either improved exciton extraction efficiency or reduced BT, we undertook further investigations to better understand the full nature of the origins of the device improvement.

PbS Photoluminescence Quenching Measurements and Back Transfer Alleviation Calculations:

To investigate this ligand-effect hypothesis further, we measured the extraction efficiency of excitons from PbS (i.e., φ_{ET1}). We measured this efficiency by observing the changes in PbS photoluminescence (PL) in various device configurations (see Figure 3b). To start, we measured the PL of PbS-only films (black curve in Figure 3a) upon 808 nm excitation. Under the same excitation intensity, we measured the PL of PbS films with (1) rubrene/DBP evaporated on top (orange curve), (2) 3 mM TCA and rubrene/DBP (blue curve), and (3) 6 mM TCA and rubrene/DBP (yellow curve). By integrating the PbS emission curve and using Equation 4, we calculated the quenching efficiency of these different configurations. We note that our measurement of φ_{ET1} is an approximation as there are changes to the optical outcoupling and non-radiative pathways that are introduced when the organic layers are deposited onto the PbS film.

$$\varphi_{ET1} = 100 \times \frac{\text{(neat PbS film emission-UC film PbS emission)}}{\text{Neat PbS film emission}} \qquad \text{Equation 4}$$

Promisingly, we observed an increase in quenching efficiency with increasing TCA concentrations (see Figure 3c). For all concentrations of PbS, without the introduction of TCA, less than 80% of the PbS emission is quenched (orange bars in Figure 3c). In stark contrast, the PbS emission from 5 and 10 mg/mL PbS films are almost completely quenched when 3 or 6 mM TCA is introduced as an interlayer between PbS and rubrene (blue and yellow bars in Figure 3c). In particular, we note that for 50 mg/mL PbS films, the quenching efficiency rises from approximately 75% to over 85% upon the introduction of 6 mM TCA. This increased quenching efficiency with the introduction of TCA provides evidence of an increase in the Dexter energy transfer efficiency (φ_{ET1}) from PbS to the organic layers.

Although there is an improvement in Dexter energy transfer efficiency from QDs upon introduction of the TCA layer, this improvement accounts for only a small fraction of the improvement in EQE. Using Equation 2, we calculated the percent improvement in the remaining φ_{ET2} x (1 – φ_{BT}) term which includes the improvements resulting from back transfer alleviation (see Figure 3d). For this calculation, we used our measured values for EQE, φ_{ET1}, and DBP/rubrene PLQY (~38%), and we assumed the φ_{TTA} to be 31% based on measurements from Di et al.[44,50,80] We note that there may be minor changes in φ_{TTA} upon introduction of TCA as an interlayer due to changes in rubrene crystallization. [81,82] Under the assumption of minimal changes in φ_{TTA}, we found that there are massive improvements in the φ_{ET2} x (1 – φ_{BT}) term, especially at thicker PbS QD films (see Figure 3d). For all thicknesses of PbS films, we observe a significant increase in the φ_{ET2} x (1 – φ_{BT}) term upon the introduction of 3 mM TCA. With increasing PbS film thickness, the decline in $\varphi_{ET2} \times (1-\varphi_{BT})$ is substantial for samples without TCA (orange bars), while the decline is significantly mitigated for 3 mM and 6 mM TCA samples (blue and yellow bars in Figure 3d). This is likely due to the spatial separation of the donor (rubrene/DBP) and acceptor (PbS QDs) in the FRET-based energy transfer using 3 mM (~10 nm thickness) and 6 mM TCA (~18 nm thickness).

In Figure 3e, we summarize these results by plotting the percent improvement in the $\varphi_{ET2} \times (1-\varphi_{BT})$ term and the φ_{ET1} term for different PbS concentrations. The contributions from triplet extraction decrease with an increase in PbS thickness. Meanwhile, the improvements in the $\varphi_{ET2} \times (1-\varphi_{BT})$ term increase sharply with PbS concentration. There is a nearly (2500 ± 500)% improvement in the $\varphi_{ET2} \times (1-\varphi_{BT})$ term while there is a (4 ± 2)% improvement in the φ_{ET1} term for 50 mg/mL PbS films. This suggests that the issues of back energy transfer to PbS QDs are far more severe for thicker PbS films, resulting in larger improvements in EQE upon the introduction of TCA as a blocker layer. By successfully addressing the bottleneck of back energy transfer while maintaining forward energy transfer, we are able to achieve manyfold higher IQEs for strongly absorbing UC films.

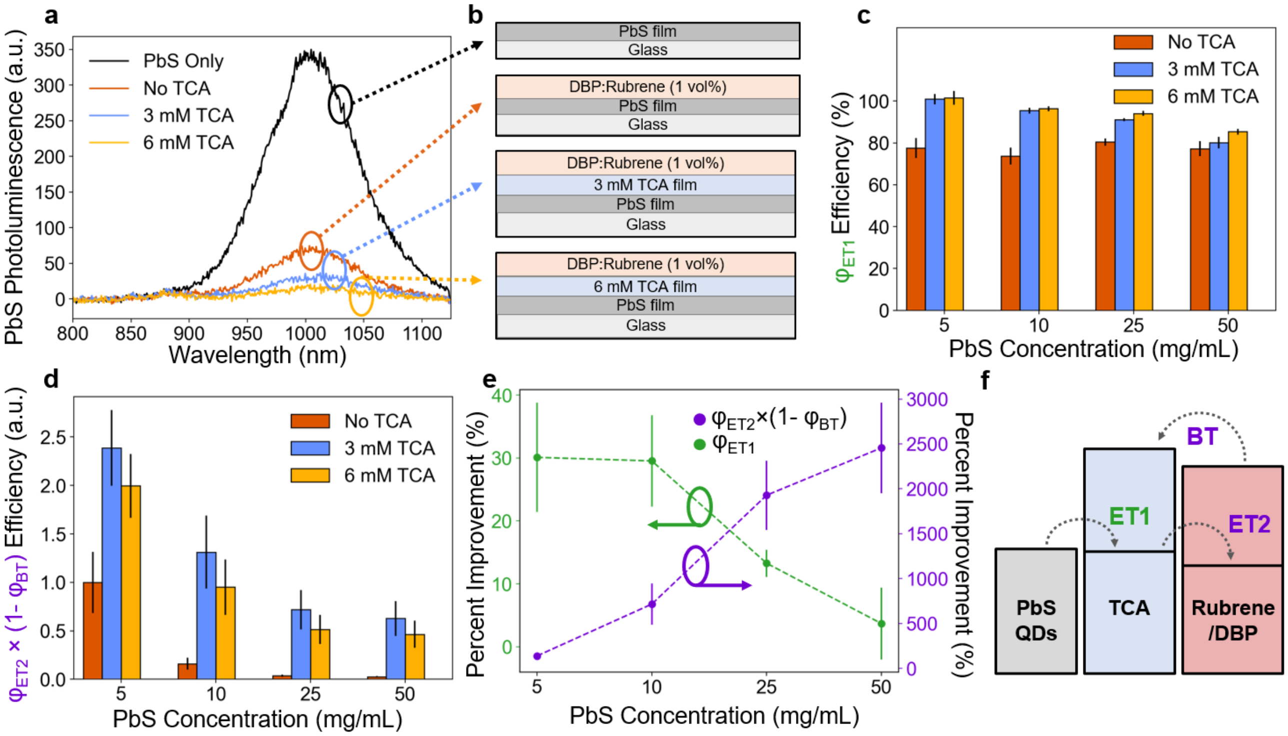

Figure 3: **(a)** Emission spectra of different film stacks to calculate PbS QD quenching efficiencies (φ_{ET1}). **(b)** Schematics of the film stacks fabricated. **(c)** Efficiency of [φ_{ET1}] and **(d)** relative efficiency of [φ_{ET2} * (1- φ_{BT})] as functions of TCA and PbS concentrations. **(e)** Percent improvement of [φ_{ET1}] and [φ_{ET2} * (1- φ_{BT})] of 3 mM TCA devices (with respect to non-TCA devices) as a function of PbS concentration. **(f)** Schematic highlighting the key energy transfer steps ET1, ET2, and BT.

Anti-Counterfeiting Demonstration:

Given the achieved EQE improvements, we explored applications to demonstrate the practical use of this new device architecture. Due to the contrasting UC performance between samples with and without TCA upon NIR excitation and the potential to pattern the TCA layer, anti-counterfeiting was particularly attractive to us. We found that the thermal deposition of TCA (~12 nm) shows the same improvements as we observed *via* solution-processing. We patterned the TCA layer using a shadow mask (see Figure 4a) followed by rubrene/DBP evaporation on the entire substrate (i.e., without a mask). Upon NIR excitation, we observed a strong contrast between TCA- and non-TCA-patterned areas.

As shown in Figure 4, we developed a simple, configurable method to uniformly pattern images for personalized anti-counterfeiting. We fabricated devices with the Stanford University logo, the Stanford Bunny, the outline of the Stanford Memorial Church, and a simplified Congreve Lab logo upon excitation with an 850 nm LED. We captured clear pictures of the upconverted images under room lighting (see Figure SI 11) with low excitation intensities between 10 and 100 mW/cm^2.

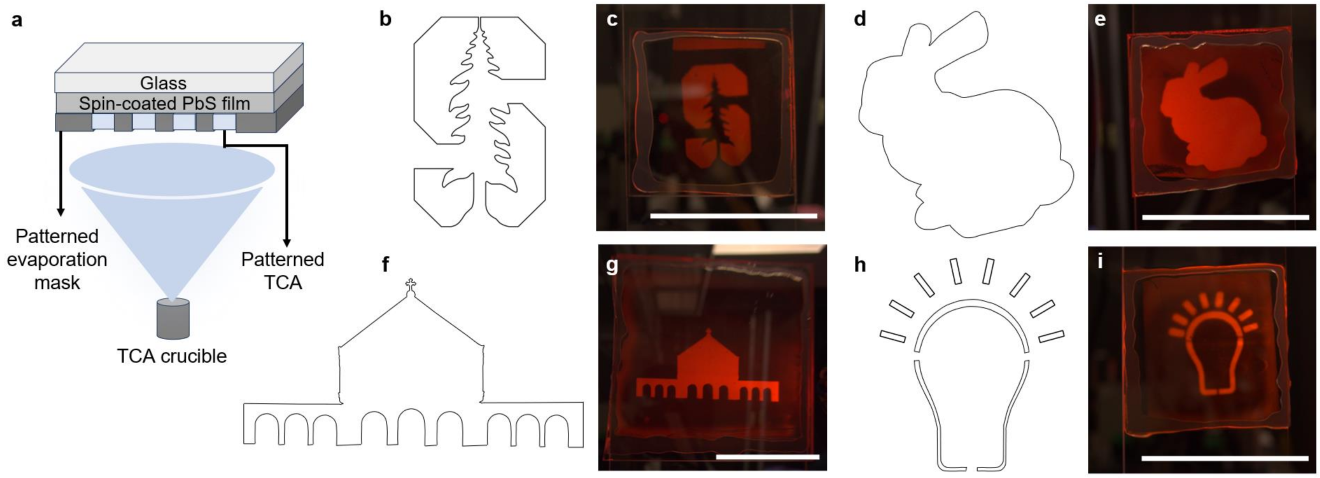

Figure 4: **(a)** Schematic illustration of patterning of TCA layer *via* thermal deposition. Images for evaporation mask laser cutting: **(b)** Stanford logo, **(d)** Stanford Bunny, **(f)** Stanford Memorial Church outline, **(h)** Congreve Lab logo outline. Unedited images of upconversion under 850 nm LED illumination with 200 millisecond exposure time: **(c)** Stanford logo, **(e)** Stanford Bunny, **(g)** Memorial Church outline, **(i)** Bulb outline from Congreve Lab logo. The scale bar is 1 inch in length.

Discussion:

We alleviated three issues plaguing the conventional NIR-to-visible upconverting PbS-rubrene/DBP devices: (1) low absorption of NIR photons, (2) low energy transfer rates from PbS to rubrene/DBP, and (3) highly parasitic back transfer (BT) from rubrene/DBP to PbS. Upon incorporation of 5-tetracene carboxylic acid as a blocker layer, we achieved a champion UC EQE of 0.011% with average peak EQEs of (0.010 ± 0.001)% at 5.3 W/cm^2 of 808 nm excitation. We uncovered the mechanism of EQE improvement, finding the back-transfer alleviation to be the primary source, especially for thicker PbS films. We believe this demonstration functions as a proof of concept of a device architecture which can be broadened to other upconversion systems to improve EQEs in the solid- state for practical incorporation in real-world applications. Additionally, the EQE improvement in this NIR-to-visible regime is a key step towards the realization of TTA-UC in photovoltaics, night vision, and anti-counterfeiting technologies. This demonstration functions as a proof of concept of a device architecture which can be applied to other solid-state UC systems to improve efficiencies for practical incorporation in real-world applications.

Methods:

Materials:

Rubrene (>99.0%, purified by sublimation) was purchased from TCI America. 5-tetracene carboxylic acid (>95% by NMR) was purchased from HAARES ChemTech Inc. PbO (Puratronic^{TM}, 99.999%, metals basis), 1-octadecene (90%, technical grade), anhydrous toluene (99.85%, extra dry over molecular sieves, AcroSeal), and anhydrous acetonitrile (99.9+%, extra dry, AcroSeal) were purchased from Thermo Scientific Chemicals. Oleic acid (technical grade, 90%), DBP (5,10,15,20-Tetraphenylbisbenz[5,6]indeno[1,2,3-cd:1′,2′,3′-lm]perylene, 98% HPLC), and hexamethyldisilathiane (synthesis grade) were purchased from Millipore Sigma. Hexanes (certified ACS), isopropanol (ACS certified), and acetone (ACS certified) were purchased from Fisher Scientific. All chemicals were used as purchased unless specified.

Synthesis of PbS quantum dots (930 nm absorption peak):

PbS quantum dots were fabricated using a modified Hines hot-injection technique.[60, 83] To a two-neck 100 mL round bottom, 0.669 g of PbO, 30 mL of 1-octadecene, and 2 mL of oleic acid were added. The flask was heated under vacuum to degas and synthesize lead oleate (temperature was increased to 120 °C slowly at 10 °C every 10 minutes). The reaction flask was degassed at 120 °C for at least 4 hours resulting in a clear solution. The injection temperature was set to 105 °C and the flask was refilled with nitrogen. In a nitrogen atmosphere glovebox, 7.5 mL of dry toluene was charged with 350 µL of hexamethyldisilathiane. This solution was removed from the glovebox (<0.1 ppm O_2, <0.5 ppm H_2O) and injected into the reaction flask with minimal exposure to air. Upon injection, the reaction flask was immediately removed from the heat plate and allowed to air cool. Upon reaching room temperature, the reaction was washed with acetone (4x volume of acetone was added and centrifuged at 8800xg for 2 mins). The resulting pellet was redispersed in hexanes (~30 mL) and washed with acetone (x4 volume of acetone was added and centrifuged at 8800xg for 2 mins). The final pellet was redispersed in hexanes (~15 mL) and stored in the glovebox until use.

Fabrication of upconversion devices:

Substrate treatment: All samples, unless otherwise specified, are fabricated on 1 cm x 1 cm soda-lime glass of thickness 1.1 mm. All substrates were washed by sonicating for 10 minutes in a 1% Hellmanex detergent solution in deionized water, followed by two 5-minutes sonications in deionized water, followed by two 5-minute sonications in acetone, and two 5-minute sonications in isopropanol. The substrates were then dried under pressurized air to remove solvent and dust particles. Within 15 minutes before spin coating, the glass substrates were treated with UV ozone plasma for at least 15 minutes.

Solution preparation: The PbS QDs stock solution was washed with acetone once more (4x acetone, 8800 rcf for 2 mins) to create a pellet. In a nitrogen-filled glovebox, this weighed pellet was dissolved in anhydrous toluene to make the solutions with the desired concentrations (5, 10, 25, 50 mg/mL *via* serial dilution) and filtered through 0.2 μm PTFE membrane syringe filters (Titan3, 17mm, filter blue) before spin coating. In a nitrogen-filled glovebox, a 10 mM stock solution of TCA in anhydrous acetonitrile was prepared by heating the solution at ~70 °C overnight. After cooling, the resulting solution was filtered through Titan3, 17mm, filter blue 0.2 μm PTFE membrane syringe filters and diluted as needed (3 mM or 6 mM TCA in acetonitrile) before spin coating.

Spin coating: All spin coating was performed in a nitrogen-filled glovebox. PbS QD solutions in toluene (80 μL) were spin-coated at 1500 rpm for 30 seconds with a 0.8 second ramp (1,875 rpm/s ramp). TCA solutions in acetonitrile (100 μL) were spun on top of the PbS QD film with the same spin conditions. After the spin(s), the substrates were annealed on a hot plate at 70 °C for 15 minutes.

Thermal evaporation: The spin coated substrates were then loaded into an Angstrom Engineering thermal evaporation chamber. All evaporations were performed under a pressure of less than 1E-05 mbar. DBP-doped (1% v/v) rubrene evaporations were performed by co-evaporating the chemicals from two different sources. For a 1% doping, the DBP was evaporated at a rate of ~0.02-0.03 Å/s while the rubrene was evaporated at ~2-3 Å/s. Both DBP and rubrene were evaporated from resistively heated alumina crucibles. The rubrene/DBP films had a final thickness of ~64 nm based on profilometry. This rubrene thickness showed the best performance for our UC devices.

Encapsulation: All samples were encapsulated with a 1.2 mm-thick microscope slide (Electron Microscopy Sciences) using Norland Optical NOA81 (Thorlabs) fast curing optical adhesive cured under a UV-lamp for 2 minutes.

Photoluminescence quantum yield (PLQY) measurement: Photoluminescence quantum yields of rubrene/DBP films were measured using the de Mello method in an integrating sphere (from Labsphere).[84] The integrating sphere was calibrated using a radiometric light source (HL-3P-INT-CAL, Ocean Insight). A 447 nm continuous wave laser was used to excite the neat rubrene/DBP (~64 nm) films. The sample was loaded into the sphere such that the 447 m laser had an approximately 8-degree incidence.

Steady-state photoluminescence and UC photoluminescence measurement: All relative PL and UCPL measurements were conducted on the set up shown in SI Figure 6. The samples were illuminated with an 808 nm continuous wave laser at an angle of ~45 degrees. The emission from the samples was collected using a high NA lens and fiber-coupled spectrometer (QE pro high-performance, Ocean Insight). The fiber coupling to the detector included a filter holder. A 750 nm short pass filter (Thorlabs) was used to filter the laser out of the UCPL spectra. An 850 nm long pass filter (Thorlabs) was used to filter the laser out of the PbS QD PL spectra.

To calculate upconversion photoluminescence, the emission was integrated from 500-700 nm. To calculate the PbS photoluminescence, the emission was integrated from 900-1100 nm. Integration times and scans to average were adjusted to achieve high signal-to-noise ratios.

Upconversion external quantum efficiency measurement: To measure the EQEs, the method introduced by Izawa et al. was used.[44] The photoluminescence set up described above was used for this measurement. A rubrene/DBP-only film (~64 nm) was used as the standard with a known PLQY (measured in the integrating sphere as described above). The PL (integrated 500-700 nm) from rubrene/DBP-only samples (I_{std}) was measured using a 447 nm continuous wave laser. With the same optical alignment, the UCPL (integrated 500-700 nm) from upconversion devices (I_{UC}) was measured using an 808 nm continuous wave laser with an intensity of 5.3 W/cm^2. The incident power of the 447 nm (P_{std}) and 808 nm (P_{UC}) lasers were measured using a Thorlabs power meter (PM100D meter with S120VC sensor). All measurements were performed with a 750 nm short pass filter (Thorlabs). For each device stack, triplicates were fabricated and 4 points on each sample were measured with random positions. The resulting averages and standard deviations were propagated using the Python uncertainties package. Equation 5 was used to calculate the EQEs of the different devices.

$$\mathrm{EQE} = \frac{I_{UC}}{I_{Std}} \times \frac{P_{Std}}{P_{UC}} \times (\%A_{Std}) \times \mathrm{PLQY}_{Std} \qquad \text{Equation 5}$$

PbS photoluminescence quenching measurement: The photoluminescence setup was used with an 850 nm long pass filter (Thorlabs) to perform measurements of PbS PL (integrated from 900-1100 nm). The devices were excited using an 808 nm laser at 0.56 W/cm^2 intensity. Each device stack was prepared in triplicates and 4 measurements were performed on each substrate randomly. The resulting averages and standard deviations were propagated using the python uncertainties package. Quenching efficiencies were calculated using Equation 4. PbS-only films were used to calculate PL_{PbS}, while PbS-rubrene/DBP and PbS-TCA-rubrene/DBP films were used to calculate PL_{UC}.

Upconversion threshold measurement: Upconversion threshold was measured using the photoluminescence set up described above. The laser was set to the highest power required for the measurement and the power was attenuated using ND filters. The UC PL for the samples was measured across orders of magnitude of input power to span the linear and quadratic regimes in the log-log input-output power plots. The integration times were increased to achieve high signal at low input powers.

The input power for each point was measured using a Thorlabs power meter (PM100D meter with S120VC sensor). The spot-size of the input laser was measured using a camera to calculate the intensity of the input light. The threshold intensity was calculated by fitting the log-log plot in the linear and quadratic regimes to find the abscissa of the point of intersection of those lines.

Note: The upconversion threshold was measured for 5 mg/mL PbS with and without 3 mM TCA. This was because with thicker PbS (25 and 50 mg/mL), there was insufficient UC signal from the control (no TCA) samples to measure the threshold. The same samples (5 mg/mL with and without 3 mM TCA) were used to measure the TRUCPL.

Spot-size measurement: Spot-sizes were calculated using a Zelux 1.6 MP Color CMOS camera. ND filters were used to prevent saturation of the camera. The full width at half maximum was calculated. Since the measurements were performed at 45-degree incidence, an ellipsoidal area was calculated from the spot-size.

Time-resolved upconversion photoluminescence spectroscopy measurement: The TRUCPL decays were collected using a Streakscope C10627 from Hamamatsu Corp. A Dragon Laser H Series 808 nm was pulsed by a function generator RIGOL DG812.

UV-vis spectroscopy (absorption) measurement: UV-vis spectroscopy was performed on 50 mg/mL PbS films (encapsulated) using an Agilent Cary 6000i UV/vis/NIR machine in transmission mode. For solution-state measurements, a 1 cm path length quartz cuvette was used. The PbS QDs solution-state absorption was measured in hexanes with a baseline of the absorption of hexanes neat. We also used a second relative method to calculate the absorption values, which resulted in similar values (see SI for more information).

Atomic force microscopy measurement: The AFM images were taken in ambient air by NX-10 in non-contact mode. The film (5 mg/mL with 6 mM TCA) was cut using a blade to measure the thickness.

Profilometry measurement: A Dektak XT-S Stylus profilometer was used under 3 mg stylus force, with grooves scratched into the samples with a razor blade for measurement.

Fabrication of evaporation masks: Evaporation masks were fabricated through laser cutting of aluminum metal sheets using FabLight FL4500.

Fabrication of anti-counterfeiting devices: This fabrication was performed on 1 inch x 1 inch or 2 inch x 2 inch (for the Stanford Memorial Church image) soda-lime glass substrates. These substrates were washed and treated as described above. While spin coating, 350 uL of 10 mg/mL PbS QD solution was used. Instead of spin coating TCA in acetonitrile, neat TCA was thermally evaporated onto the PbS QD film through a shadow mask at a rate of 1-3 Å/s from a resistively heated crucible. The rubrene/DBP was then evaporated onto the entire substrate without a mask. The devices were encapsulated using EpoTek UV-curing epoxy glue.

Imaging of anti-counterfeiting devices: An 850 nm LED from Thorlabs (M850L3) was used as the excitation source. A camera (Kiralux 8.9 MP Color CMOS Camera) was mounted with an imaging lens to take pictures of the substrates. Images were taken under 200 ms exposure time. See SI Figure 11. Excitation power was measured using a power meter (PM100D meter with S120VC sensor). NOTE: the image of Memorial Church was taken under waveguided excitation due to the large size (2 inch x 2 inch) of the substrate.

Acknowledgements:

Funding from the Defense Advanced Research Projects Agency grant HR00112220010 (PN, MH, EB, LP, GA, DF, RH, MK, DC) is acknowledged. Part of this work was performed at the Stanford Nano Shared Facilities (SNSF), supported by the National Science Foundation under award ECCS-2026822. Part of this work was performed at Lab64, the EE Makerspace at Stanford University. We would like to acknowledge the Stanford Computer Graphics Laboratory for the Stanford Bunny image. PN acknowledges the support of a Stanford Graduate Fellowship in Science & Engineering (SGF) as a Gabilan Fellow and the Chevron Fellowship in Energy. MH acknowledges the support of the Department of Electrical Engineering at Stanford University. AOG acknowledges the support of a National Science Foundation Graduate Research Fellowship under grant DGE-1656518 and a Stanford Graduate Fellowship in Science & Engineering (SGF) as a Scott A. and Geraldine D. Macomber Fellow. LP acknowledges support of a National Science Foundation Graduate Research Fellowship under grant DGE-2146755. THS acknowledges the support of the Arnold O. Beckman Postdoctoral Fellowship. SF acknowledges the support from Stanford University as a Diversifying Academia, Recruiting Excellence (DARE) Fellow, the U.S. Department of Energy (DOE) Building Technologies Office (BTO) as an IBUILD Graduate Research Fellow, Stanford Graduate Fellowship in Science & Engineering (SGF) as a P. Michael Farmwald Fellow, and of the National GEM Consortium as a GEM Fellow. KMKY acknowledges the Chevron Energy Fellowship and the Stanford DARE fellowship for partial support. TFJ and KMKY acknowledge support from the Liquid Sunlight Alliance, which is supported by the U.S. Department of Energy, Office of Science, Office of Basic Energy Sciences, Fuels from Sunlight Hub under Award Number DE-SC0021266 for template design for system demonstration. WM and NM acknowledge support from the Stanford University Department of Electrical Engineering through the Research Experience for Undergraduates (REU) program. VM acknowledges support from the Stanford University School of Engineering through the Stanford Undergraduate Research Fellowship (SURF) program. RH acknowledges the support of Chancellor’s Opportunity Fellowship. This research was performed under an appointment to the Building Technologies Office (BTO) IBUILD Graduate Research Fellowship administered by the Oak Ridge Institute for Science and Education (ORISE) and managed by Oak Ridge National Laboratory (ORNL) for the DOE. ORISE is managed by Oak Ridge Associated Universities (ORAU). All opinions expressed in this paper are the authors' and do not necessarily reflect the policies and views of the DOE, EERE, BTO, ORISE, ORAU, or ORNL.

Author contributions:

Conceptualization: PN, MH, GA, EB, DNC. Methodology: PN, MH, AOG, QZ. Investigation and interpretation: PN, MH, AOG, LP, QZ, EB, GA, SF, WM, NM, VM, DF, RH, THS, KMKY. Supervision: TFJ, MAK, DNC. Writing - original draft: PN. Writing - review and editing: all authors. Funding acquisition: MAK, DNC.

References:

1. Carrod, A. J., Gray, V. & Börjesson, K. Recent advances in triplet–triplet annihilation upconversion and singlet fission, towards solar energy applications. *Energy Environ Sci* **15**, 4982–5016 (2022).
2. Schulze, T. F. *et al.* Efficiency enhancement of organic and thin-film silicon solar cells with photochemical upconversion. *Journal of Physical Chemistry C* **116**, 22794–22801 (2012).
3. Goldschmidt, J. C., Fischer, S., Goldschmidt, J. C. & Fischer, S. Upconversion for Photovoltaics – a Review of Materials, Devices and Concepts for Performance Enhancement. *Adv Opt Mater* **3**, 510–535 (2015).
4. Singh, R. *et al.* Harvesting Sub-bandgap Photons via Upconversion for Perovskite Solar Cells. *ACS Appl Mater Interfaces* **13**, 54874–54883 (2021).
5. Kinoshita, M. *et al.* Photon Upconverting Solid Films with Improved Efficiency for Endowing Perovskite Solar Cells with Near-Infrared Sensitivity. *ChemPhotoChem* **4**, 5271–5278 (2020).
6. Liu, S.-W. *et al.* Transparent Organic Upconversion Devices for Near-Infrared Sensing. *Advanced Materials* **27**, 1217–1222 (2015).
7. Ravetz, B. D. *et al.* Photoredox catalysis using infrared light via triplet fusion upconversion. *Nature 2019 565:7739* **565**, 343–346 (2019).
8. Pfund, B. *et al.* UV Light Generation and Challenging Photoreactions Enabled by Upconversion in Water. *J Am Chem Soc* **142**, 10468–10476 (2020).
9. Huang, L. *et al.* Highly effective near-infrared activating triplet-triplet annihilation upconversion for photoredox catalysis. *J Am Chem Soc* **142**, 18460–18470 (2020).
10. Hagstrom, A. L., Weon, S., Choi, W. & Kim, J. H. Triplet-Triplet Annihilation Upconversion in Broadly Absorbing Layered Film Systems for Sub-Bandgap Photocatalysis. *ACS Appl Mater Interfaces* **11**, 13304–13318 (2019).

11. Askes, S. H. C. & Bonnet, S. Solving the oxygen sensitivity of sensitized photon upconversion in life science applications. *Nature Reviews Chemistry 2018 2:12* **2**, 437–452 (2018).

12. Kwon, O. S. *et al.* Dual-color emissive upconversion nanocapsules for differential cancer bioimaging in vivo. *ACS Nano* **10**, 1512–1521 (2016).

13. Mattiello, S. *et al.* Self-Assembled Dual Dye-Doped Nanosized Micelles for High-Contrast Up-Conversion Bioimaging. *Adv Funct Mater* **26**, 8447–8454 (2016).

14. Wohnhaas, C. *et al.* Annihilation Upconversion in Cells by Embedding the Dye System in Polymeric Nanocapsules. *Macromol Biosci* **11**, 772–778 (2011).

15. Liu, Q., Yang, T., Feng, W. & Li, F. Blue-emissive upconversion nanoparticles for low-power-excited bioimaging in vivo. *J Am Chem Soc* **134**, 5390–5397 (2012).

16. Liu, Q. *et al.* A General Strategy for Biocompatible, High-Effective Upconversion Nanocapsules Based on Triplet–Triplet Annihilation. *J Am Chem Soc* **135**, 5029–5037 (2013).

17. Liu, Q. *et al.* Highly Photostable Near-IR-Excitation Upconversion Nanocapsules Based on Triplet-Triplet Annihilation for in Vivo Bioimaging Application. *ACS Appl Mater Interfaces* **10**, 9883–9888 (2018).

18. You, M. *et al.* Inkjet printing of upconversion nanoparticles for anti-counterfeit applications. *Nanoscale* **7**, 4423–4431 (2015).

19. Yin, W. *et al.* Thermally Activated Upconversion with Metal-Free Sensitizers Enabling Exceptional Anti-Stokes Shift and Anti-counterfeiting Application. *ACS Appl Mater Interfaces* **13**, 57481–57488 (2021).

20. Suo, H. *et al.* High-security anti-counterfeiting through upconversion luminescence. *Materials Today Physics* **21**, 100520 (2021).

21. Sanders, S. N. *et al.* Triplet fusion upconversion nanocapsules for volumetric 3D printing. *Nature 2022 604:7906* **604**, 474–478 (2022).

22. Limberg, D. K., Kang, J. H. & Hayward, R. C. Triplet-Triplet Annihilation Photopolymerization for High-Resolution 3D Printing. *J Am Chem Soc* **144**, 5226–5232 (2022).

23. O'dea, C. J., Isokuortti, J., Comer, E. E., Roberts, S. T. & Page, Z. A. Triplet Upconversion Under Ambient Conditions Enables Digital Light Processing 3D Printing. (2023) doi:10.26434/CHEMRXIV-2023-F1QHQ.

24. Wong, J. *et al.* Triplet Fusion Upconversion for Photocuring 3D-Printed Particle-Reinforced Composite Networks. *Advanced Materials* **35**, 2207673 (2023).

25. Schloemer, T. *et al.* Nanoengineering Triplet-Triplet Annihilation Upconversion: From Materials to Real-World Applications. *ACS Nano* **17**, 3259–3288 (2023).

26. Rauch, M. P. & Knowles, R. R. Applications and Prospects for Triplet–Triplet Annihilation Photon Upconversion. *Chimia (Aarau)* **72**, 501 (2018).

27. Zhou, J., Liu, Q., Feng, W., Sun, Y. & Li, F. Upconversion luminescent materials: Advances and applications. *Chem Rev* **115**, 395–465 (2015).

28. Seo, S. E. *et al.* Recent advances in materials for and applications of triplet–triplet annihilation-based upconversion. *J Mater Chem C Mater* **10**, 4483–4496 (2022).

29. Ji, Y. *et al.* Huge upconversion luminescence enhancement by a cascade optical field modulation strategy facilitating selective multispectral narrow-band near-infrared photodetection. *Light: Science & Applications 2020 9:1* **9**, 1–12 (2020).

30. Liang, G. *et al.* Recent progress in the development of upconversion nanomaterials in bioimaging and disease treatment. *Journal of Nanobiotechnology 2020 18:1* **18**, 1–22 (2020).

31. Borse, S., Rafique, R., Murthy, Z. V. P., Park, T. J. & Kailasa, S. K. Applications of upconversion nanoparticles in analytical and biomedical sciences: a review. *Analyst* **147**, 3155–3179 (2022).

32. Duan, C., Liang, L., Li, L., Zhang, R. & Xu, Z. P. Recent progress in upconversion luminescence nanomaterials for biomedical applications. *J Mater Chem B* **6**, 192–209 (2018).

33. Upconversion Nanomaterials in Bioimaging, T., Applications, B., Gerelkhuu, Z., Lee, Y.-I. & Hyun Yoon, T. Upconversion Nanomaterials in Bioimaging and Biosensor Applications and Their Biological Response. *Nanomaterials 2022, Vol. 12, Page 3470* **12**, 3470 (2022).

34. Auzel, F. Upconversion and Anti-Stokes Processes with f and d Ions in Solids. *Chem Rev* **104**, 139–173 (2004).

35. Lee, C. *et al.* Giant nonlinear optical responses from photon-avalanching nanoparticles. *Nature 2021 589:7841* **589**, 230–235 (2021).

36. Weingarten, D. H. *et al.* Experimental demonstration of photon upconversion via cooperative energy pooling. *Nature Communications 2017 8:1* **8**, 1–7 (2017).

37. Singh-Rachford, T. N. & Castellano, F. N. Photon upconversion based on sensitized triplet–triplet annihilation. *Coord Chem Rev* **254**, 2560–2573 (2010).

38. Huang, Z. & Lee Tang, M. Semiconductor Nanocrystal Light Absorbers for Photon Upconversion. *Journal of Physical Chemistry Letters* **9**, 6198–6206 (2018).

39. Wu, M. *et al.* Solid-state infrared-to-visible upconversion sensitized by colloidal nanocrystals. *Nature Photonics 2015 10:1* **10**, 31–34 (2015).

40. Nienhaus, L. *et al.* Speed Limit for Triplet-Exciton Transfer in Solid-State PbS Nanocrystal-Sensitized Photon Upconversion. *ACS Nano* **11**, 7848–7857 (2017).

41. Yanai, N. & Kimizuka, N. New Triplet Sensitization Routes for Photon Upconversion: Thermally Activated Delayed Fluorescence Molecules, Inorganic Nanocrystals, and Singlet-to-Triplet Absorption. *Acc Chem Res* **50**, 2487–2495 (2017).

42. Wu, T. C., Congreve, D. N. & Baldo, M. A. Solid state photon upconversion utilizing thermally activated delayed fluorescence molecules as triplet sensitizer. *Appl Phys Lett* **107**, (2015).

43. Monguzzi, A., Tubino, R., Hoseinkhani, S., Campione, M. & Meinardi, F. Low power, non-coherent sensitized photon up-conversion: modelling and perspectives. *Physical Chemistry Chemical Physics* **14**, 4322–4332 (2012).

44. Izawa, S. & Hiramoto, M. Efficient solid-state photon upconversion enabled by triplet formation at an organic semiconductor interface. *Nature Photonics 2021 15:12* **15**, 895–900 (2021).

45. Sakamoto, Y., Izawa, S., Ohkita, H., Hiramoto, M. & Tamai, Y. Triplet sensitization via charge recombination at organic heterojunction for efficient near-infrared to visible solid-state photon upconversion. *Communications Materials 2022 3:1* **3**, 1–9 (2022).

46. Zhou, Y., Castellano, F. N., Schmidt, T. W. & Hanson, K. On the Quantum Yield of Photon Upconversion via Triplet-Triplet Annihilation. *ACS Energy Lett* **5**, 2322–2326 (2020).

47. Bharmoria, P., Bildirir, H. & Moth-Poulsen, K. Triplet–triplet annihilation based near infrared to visible molecular photon upconversion. *Chem Soc Rev* **49**, 6529–6554 (2020).

48. Bossanyi, D. G. *et al.* In optimized rubrene-based nanoparticle blends for photon upconversion, singlet energy collection outcompetes triplet-pair separation, not singlet fission. *J Mater Chem C Mater* **10**, 4684–4696 (2022).

49. Wang, S.-J. *et al.* Highly Crystalline Rubrene Light-Emitting Diodes with Epitaxial Growth. *Adv Funct Mater* **33**, 2213768 (2023).

50. Hu, M. *et al.* Bulk Heterojunction Upconversion Thin Films Fabricated via One-Step Solution Deposition. *ACS Nano* **17**, 37 (2023).

51. Mahboub, M., Huang, Z. & Tang, M. L. Efficient Infrared-to-Visible Upconversion with Subsolar Irradiance. *Nano Lett* **16**, 7169–7175 (2016).

52. Weiss, R., Vanorman, Z. A., Sullivan, C. M. & Nienhaus, L. A Sensitizer of Purpose: Generating Triplet Excitons with Semiconductor Nanocrystals. *ACS Materials Au* **2**, 641–654 (2022).

53. Nienhaus, L., Wu, M., Bulović, V., Baldo, M. A. & Bawendi, M. G. Using lead chalcogenide nanocrystals as spin mixers: a perspective on near-infrared-to-visible upconversion. *Dalton Transactions* **47**, 8509–8516 (2018).

54. Duan, J. *et al.* Efficient solid-state infrared-to-visible photon upconversion on atomically thin monolayer semiconductors. *Sci Adv* **8**, 4935 (2022).

55. Dziobek-Garrett, R., Imperiale, C. J., Wilson, M. W. B. & Kempa, T. J. Photon Upconversion in a Vapor Deposited 2D Inorganic-Organic Semiconductor Heterostructure. *Nano Lett* **23**, 4837–4843 (2023).

56. Baluschev, S. *et al.* A general approach for non-coherently excited annihilation up-conversion: transforming the solar-spectrum. *New J Phys* **10**, 013007 (2008).

57. Deng, F., Sommer, J. R., Myahkostupov, M., Schanze, K. S. & Castellano, F. N. Near-IR phosphorescent metalloporphyrin as a photochemical upconversion sensitizer. *Chemical Communications* **49**, 7406–7408 (2013).

58. Radiunas, E. *et al.* Understanding the limitations of NIR-to-visible photon upconversion in phthalocyanine-sensitized rubrene systems. *J Mater Chem C Mater* **8**, 5525–5534 (2020).

59. Sasaki, Y., Yanai, N. & Kimizuka, N. Osmium Complex-Chromophore Conjugates with Both Singlet-to-Triplet Absorption and Long Triplet Lifetime through Tuning of the Heavy-Atom Effect. *Inorg Chem* **61**, 5982–5990 (2022).

60. Zhang, J. *et al.* Synthetic Conditions for High-Accuracy Size Control of PbS Quantum Dots. *Journal of Physical Chemistry Letters* **6**, 1830–1833 (2015).

61. Wu, M., Jean, J., Bulović, V. & Baldo, M. A. Interference-enhanced infrared-to-visible upconversion in solid-state thin films sensitized by colloidal nanocrystals. *Appl Phys Lett* **110**, 211101 (2017).

62. Wu, M., Lin, T. A., Tiepelt, J. O., Bulović, V. & Baldo, M. A. Nanocrystal-Sensitized Infrared-to-Visible Upconversion in a Microcavity under Subsolar Flux. *Nano Lett* **21**, 1011–1016 (2021).

63. Liao, J., Guo, W. & Luo, X. Triplet energy transfer between inorganic nanocrystals and organic molecules. *J Photochem Photobiol* **11**, 100128 (2022).

64. Gray, V. *et al.* Direct vs Delayed Triplet Energy Transfer from Organic Semiconductors to Quantum Dots and Implications for Luminescent Harvesting of Triplet Excitons. *ACS Nano* **14**, 4224–4234 (2020).

65. Alves, J., Feng, J., Nienhaus, L. & Schmidt, T. W. Challenges, progress and prospects in solid state triplet fusion upconversion. *J Mater Chem C Mater* **10**, 7783–7798 (2022).

66. Wen, S. *et al.* Future and challenges for hybrid upconversion nanosystems. *Nature Photonics 2019 13:12* **13**, 828–838 (2019).

67. Lin, B. Y. *et al.* Exciplex-Sensitized Triplet-Triplet Annihilation in Heterojunction Organic Thin-Film. *ACS Appl Mater Interfaces* **9**, 10963–10970 (2017).

68. Geva, N. *et al.* A Heterogeneous Kinetics Model for Triplet Exciton Transfer in Solid-State Upconversion. *Journal of Physical Chemistry Letters* **10**, 3147–3152 (2019).

69. Tripathi, N., Ando, M., Akai, T. & Kamada, K. Efficient NIR-to-Visible Upconversion of Surface-Modified PbS Quantum Dots for Photovoltaic Devices. *ACS Appl Nano Mater* **4**, 9680–9688 (2021).

70. Gray, V. *et al.* Triplet transfer from PbS quantum dots to tetracene ligands: is faster always better? *J Mater Chem C Mater* **10**, 16321–16329 (2022).

71. Teh, Z. L. *et al.* Enhanced Power Conversion Efficiency via Hybrid Ligand Exchange Treatment of p-Type PbS Quantum Dots. *ACS Appl Mater Interfaces* **12**, 22751–22759 (2020).

72. Huang, Z. *et al.* Enhanced Near-Infrared-to-Visible Upconversion by Synthetic Control of PbS Nanocrystal Triplet Photosensitizers. *J Am Chem Soc* **141**, 9769–9772 (2019).

73. Huang, Z. & Tang, M. L. Designing Transmitter Ligands That Mediate Energy Transfer between Semiconductor Nanocrystals and Molecules. *J Am Chem Soc* **139**, 9412–9418 (2017).

74. Lin, T.-A. *et al.* Strategies for High-Performance Solid-State Triplet–Triplet-Annihilation-Based Photon Upconversion. *Advanced Materials* **32**, 1908175 (2020).

75. Chen, C.-H. *et al.* Efficient Triplet–Triplet Annihilation Upconversion in an Electroluminescence Device with a Fluorescent Sensitizer and a Triplet-Diffusion Singlet-Blocking Layer. *Advanced Materials* **30**, 1804850 (2018).

76. Deng, Y., Jiang, L., Huang, L. & Zhu, T. Energy Flow in Hybrid Organic/Inorganic Systems for Triplet–Triplet Annihilation Upconversion. *ACS Energy Lett* **2022**, 847–861 (2022).

77. Sawa, A. *et al.* Enhancing NIR-to-visible photon upconversion in cast solid by introducing bulky substituents in rubrene and by suppressing back energy transfer. *J Mater Chem C Mater* **11**, 8502–8513 (2023).

78. Pandey, A. K. Highly efficient spin-conversion effect leading to energy up-converted electroluminescence in singlet fission photovoltaics. *Scientific Reports 2015 5:1* **5**, 1–6 (2015).

79. Luo, X. *et al.* Mechanisms of triplet energy transfer across the inorganic nanocrystal/organic molecule interface. *Nature Communications 2020 11:1* **11**, 1–10 (2020).

80. Di, D. *et al.* Efficient Triplet Exciton Fusion in Molecularly Doped Polymer Light-Emitting Diodes. *Advanced Materials* **29**, 1605987 (2017).

81. Sher, P. H. *et al.* Distinct Routes of Singlet Fission and Triplet Fusion: A Fluorescence Kinetic Study of Rubrene. *Journal of Physical Chemistry C* **123**, 3279–3284 (2019).

82. Baronas, P. *et al.* Sweet Spot of Intermolecular Coupling in Crystalline Rubrene: Intermolecular Separation to Minimize Singlet Fission and Retain Triplet-Triplet Annihilation. *Journal of Physical Chemistry C* **126**, 15327–15335 (2022).

83. Chun, X. *et al.* Colloidal PbS Nanocrystals with Size-Tunable Near-Infrared Emission: Observation of Post-Synthesis Self-Narrowing of the Particle Size Distribution. *Advanced Materials* **15**, 1844–1849 (2003).

84. Eich, II M. *et al.* An improved experimental determination of external photoluminescence quantum efficiency. *Advanced Materials* **9**, 230–232 (1997).

Supporting Information

Overcoming the Absorption Bottleneck for Solid-State Infrared-to-Visible Upconversion

Pournima Narayanan[1,2], Manchen Hu[1], Arynn O. Gallegos[1], Linda Pucurimay[1,3], Qi Zhou[1], Emma Belliveau[1], Ghada H. Ahmed[1], Sebastian Fernández[1], William Michaels[1], Natalia Murrietta[1], Vongaishe E. Mutatu[1], Demeng Feng[4], Rabeeya Hamid[4], Kyra Muk Kam Yap[5], Tracy H. Schloemer[1], Thomas F. Jaramillo[5], Mikhail A. Kats[4], Dan Congreve[1]*

[1] Department of Electrical Engineering, Stanford University, Stanford, CA 94305, USA

[2] Department of Chemistry, Stanford University, Stanford, CA 94305, USA

[3] Department of Material Science Engineering, Stanford University, Stanford, CA 94305, USA

[4] Department of Electrical and Computer Engineering, University of Wisconsin - Madison, Madison, WI 53706, USA

[5] Department of Chemical Engineering, Stanford University, Stanford, CA 94305, USA

*Corresponding author email: Congreve@stanford.edu

<u>Contents:</u>

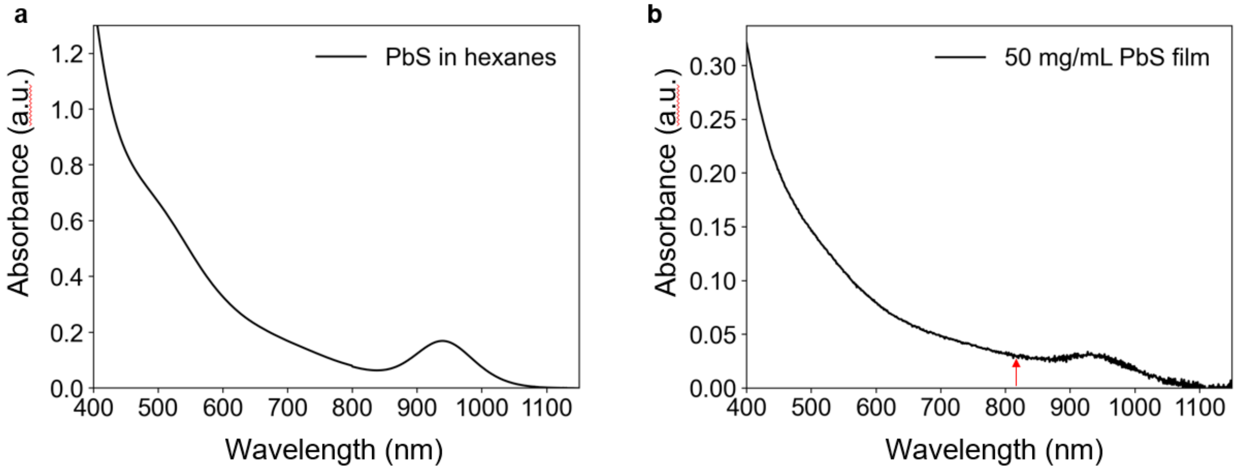

Figure SI 1: Absorption spectra of PbS QDs **(a)** in hexanes and **(b)** 50 mg/mL thin film. The red arrow in (b) highlights the 808 nm laser excitation wavelength.

Note 1: Calculating percent absorption of PbS QD films

The absorption spectrum of 50 mg/mL PbS on glass (encapsulated) was collected on a UV-vis-NIR spectrometer. After background subtracting, the absorbance at 808 nm (SI Figure 3b) was converted to percent absorption using SI equation 1. The absorption of 25, 10, and 5 mg/mL were calculated as described below.

$$\%\text{Absorption} = 100 \times (1\text{-}10^{-\text{Abs}}) \qquad \text{SI Equation 1}$$

Method 1: Percent absorption based on solid-state absorption spectrum.

The absorption spectrum of 50 mg/mL PbS QDs film was collected as described in the methods section. The absorbance at 808 nm was found to be (0.028 ± 0.004). This was converted to be (6.2 ± 0.9)% using SI equation 1.

Method 2: Percent absorption based on a comparison between solid- and solution-state absorption spectra.

The absorption spectra of 50 mg/mL PbS QDs film and a solution of PbS QDs in hexanes were collected as described in the methods section. The solid-state absorbance at 808 nm was calculated using the equation shown below to be 0.021. This was converted to be (3.0±0.4)%. We note that this is on a similar order of magnitude as the percent absorption measured using method 1.

$$\text{Abs}_{\text{solid, 808nm}} = \text{Abs}_{\text{solid, 400nm}} \times \frac{\text{Abs}_{\text{solution, 808nm}}}{\text{Abs}_{\text{solution, 400nm}}} = (0.26\pm0.03) \times \frac{(0.072\pm0.001)}{(1.4\pm0.001)}$$
$$= (0.013 \pm 0.002)$$

Note 2: Calculating percent absorption of 5, 10, 25 mg/mL PbS

The 5, 10, and 25 mg/mL films had relatively lower absorption signals than the 50 mg/mL films. To calculate the percent absorption of these films, the percent absorption of the 50 mg/mL film was scaled with the PbS thin film PL emission intensity upon 808 nm excitation of 0.56 W/cm^2 (see equation below). We observed fairly linear change in PbS PL with the change in concentration. The percent absorption of the QD films are reported below.

$$\%\mathrm{Abs}_{\mathrm{x\ mg/mL}} = \%\mathrm{Abs}_{\mathrm{50\ mg/mL}} \times \frac{\mathrm{PL}_{\mathrm{x\ mg/mL}}}{\mathrm{PL}_{\mathrm{50\ mg/mL}}}$$

%Abs Calculation Method for 50 mg/mL PbS	**5 mg/mL**	**10 mg/mL**	**25 mg/mL**	**50 mg/mL**
1	0.58±0.14	1.32±0.21	3.5±0.6	6.24±0.91
2	0.28±0.07	0.64±0.10	1.72±0.26	2.94±0.41

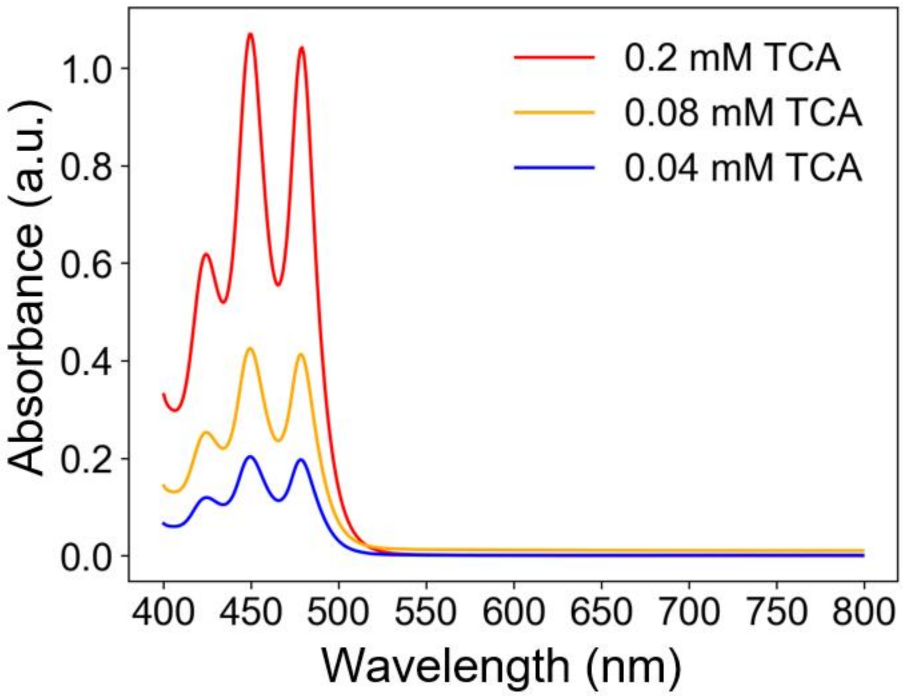

Figure SI 2: Absorbance spectra of diluted TCA solutions in acetonitrile.

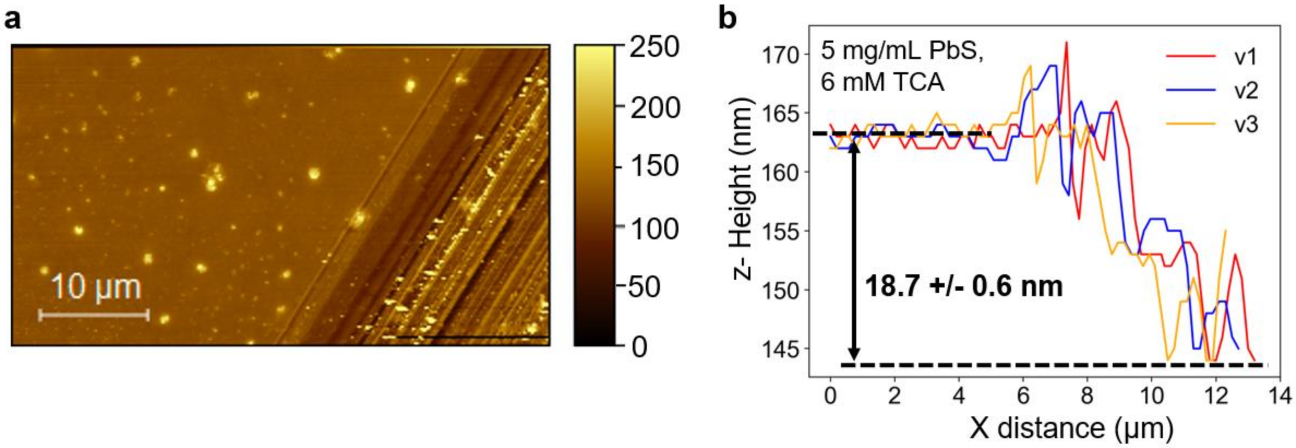

Figure SI 3: Atomic force microscopy images of a **(a)** 6 mM TCA film on top of 5 mg/mL PbS. We note that there was no perceptible thickness to 5 mg/mL PbS films alone using AFM. The film was cut with a blade to measure film thickness. Z-height profiles to calculate thicknesses for **(b)** 5 mg/mL PbS with 6 mM TCA**.** The thickness of the film was measured to be 18.7 ± 0.6 nm.

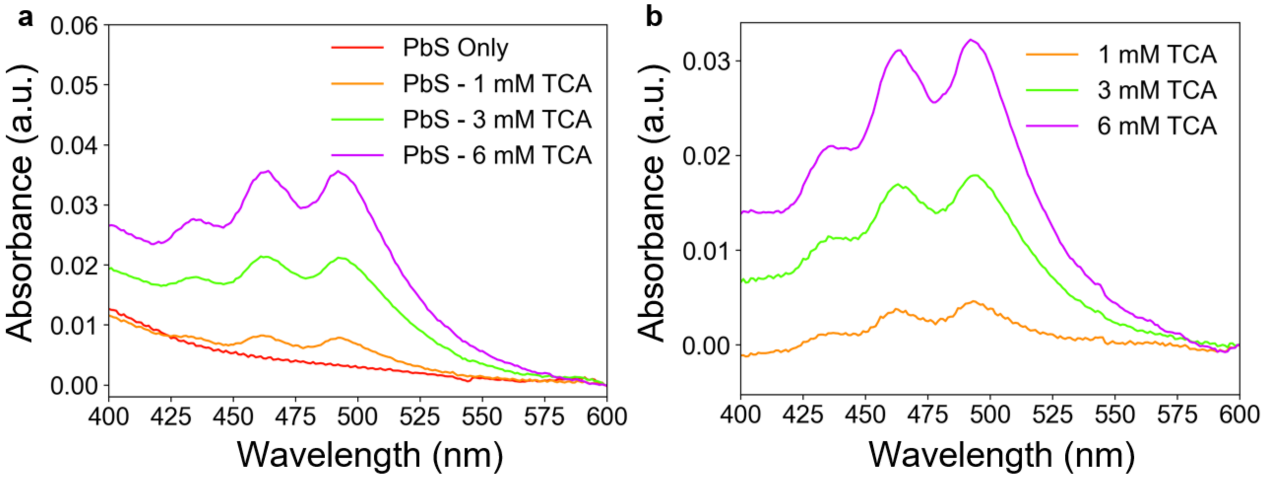

Figure SI 4: (a) Absorbance spectra of 5 mg/mL PbS films with no TCA (red), 1 mM TCA (orange), 3 mM TCA (green), and 6 mM TCA (purple). **(b)** Adjusted absorbance spectra of films with PbS absorbance subtracted.

Note 3: Calculating thicknesses of 1 and 3 mM TCA films

Based on the adjusted absorbance of the TCA films at λ_{max} of 493 nm (see Figure SI 4b) and thickness of 6 mM TCA film (see Figure SI 3b), the thicknesses of 1 and 3 mM TCA films were calculated using the below equation to be 2.7 ± 0.1 nm and 10.4 ± 0.3 nm, respectively.

$$\text{Thickness}_{\text{x mM TCA film}} = \text{Thickness}_{\text{6 mM TCA film}} \times \frac{\text{Absorbance}_{\text{x mM TCA film at 493 nm}}}{\text{Absorbance}_{\text{6 mM TCA film at 493 nm}}}$$

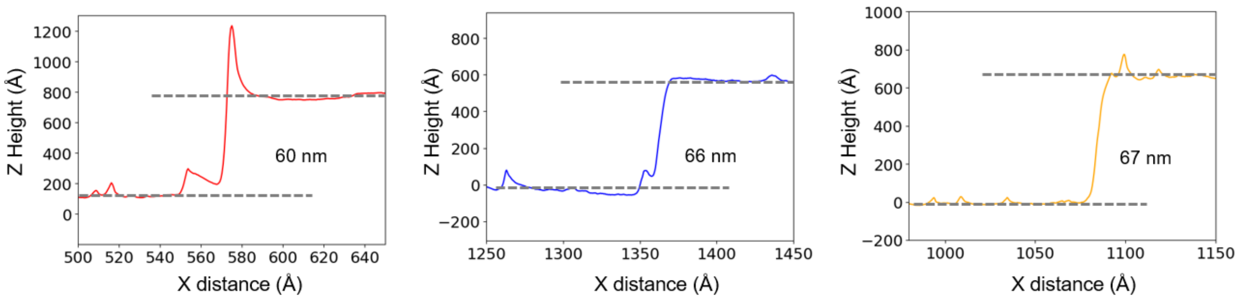

Figure SI 5: Profilometry Z height profiles for three rubrene/DBP films. Films were cut with a blade to measure film thicknesses. The average thickness was found to be 64.3 ± 3.8 nm.

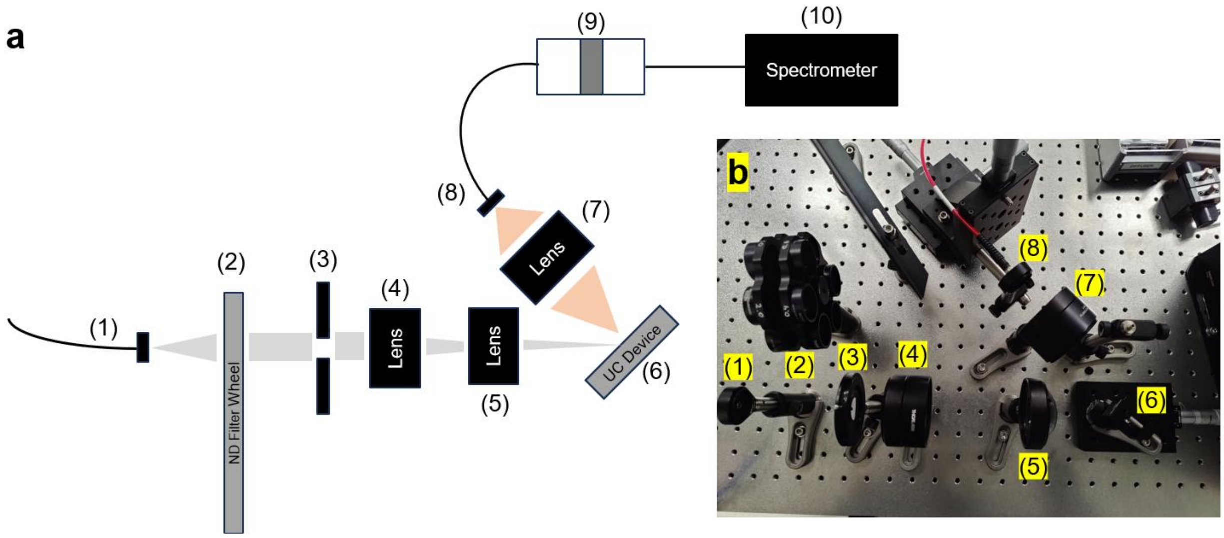

Figure SI 6: (a, b) Schematic diagram and photograph of UCPL/PL measurement setup with (1) fiber coupled 808 nm/447 nm continuous wave lasers with a filter wheel (2) and iris (3). The light is focused onto the UC device (6) at 45-degree angle using an achromatic doublet lens (4) and aspheric lens (5). The UCPL/PL is collected using a plano-convex lens (7) and focused onto a fiber-coupled spectrometer (8, 10). The light is passed through a filter (9) – 750nm SP for rubrene/DBP emission, or 850nm LP for PbS emission. The UC device is mounted on an x-stage to ensure the incident light is focused tightly. The spectrometer fiber is mounted on an XYZ stage to maximize the collection efficiency.

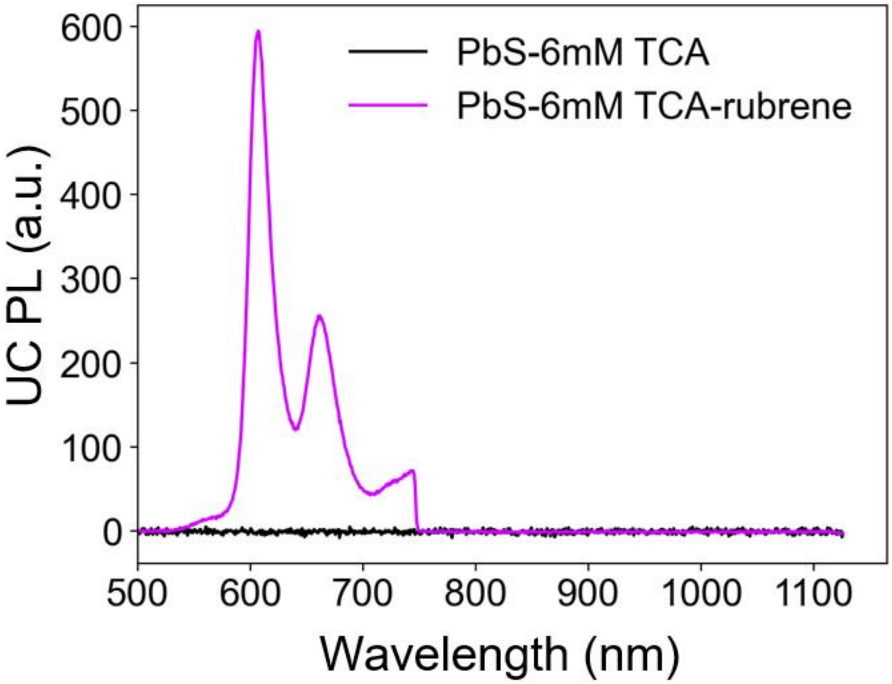

Figure SI 7: UCPL spectra for 50 mg/mL PbS film with 6 mM TCA (black trace) and 50 mg/mL PbS film with 6 mM TCA and DBP/rubrene (purple trace). The lack of UC serves as evidence that PbS and TCA alone is incapable of performing UC in the solid-state.

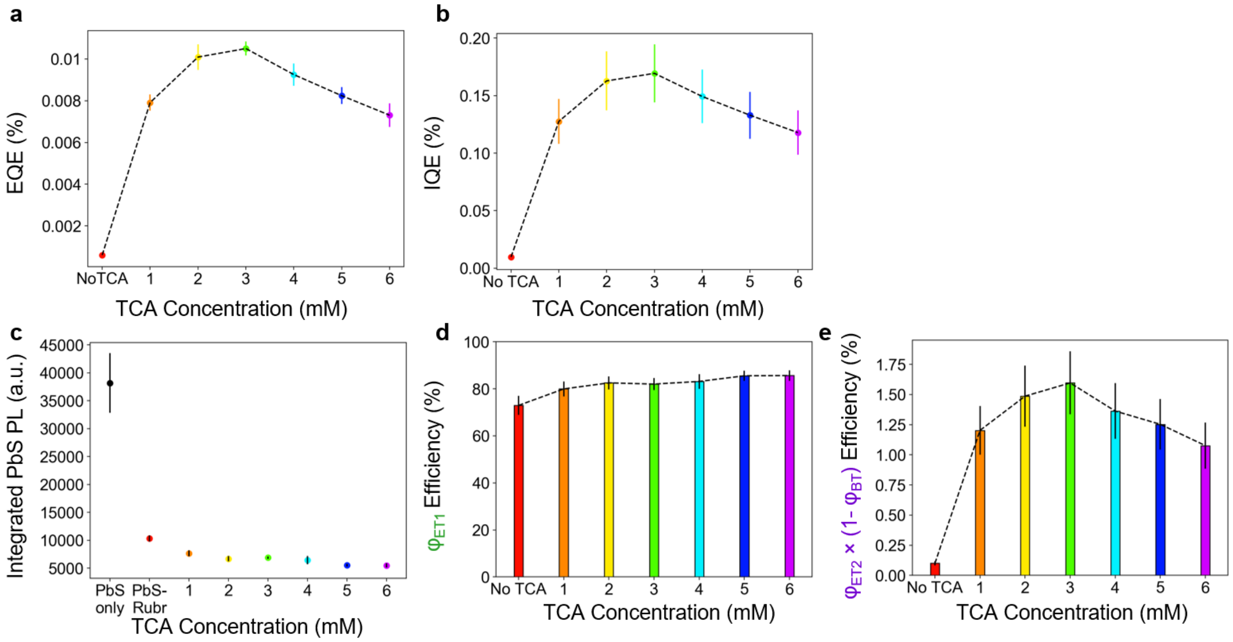

Figure SI 8: (a) TCA concentration optimization for 50 mg/mL PbS films to achieve peak EQE. **(b)** IQEs calculated at each concentration of TCA. **(c)** PbS emission counts (integrated from 900-1100 nm) upon 808 nm excitation of films. **(d)** Calculated exciton extraction efficiencies (φ_{ET1}). **(e)** Calculated $\varphi_{ET1} \times (1 - \varphi_{BT})$ efficiencies for UC devices. See the Methods section for calculation details. The dotted lines in panels a,b,d,e are added to guide the eye.

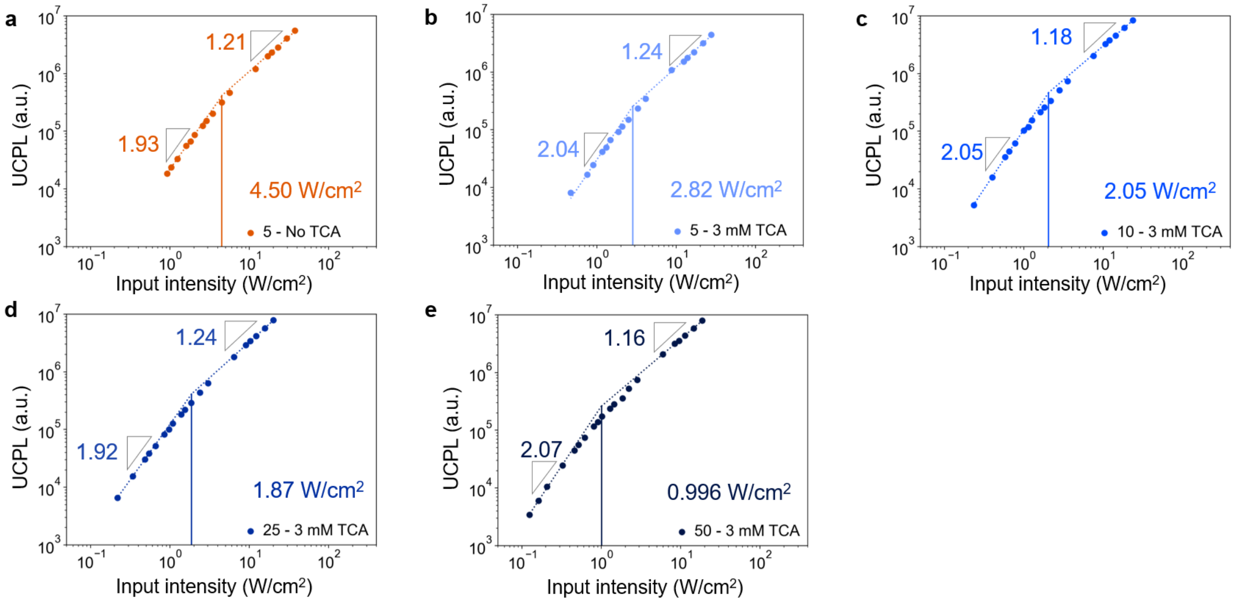

Figure SI 9: UC power dependence used to calculate the UC threshold intensities of **(a)** 5 mg/mL PbS UC device without TCA **(b)** 5 mg/mL PbS UC device with 3 mM TCA **(c)** 10 mg/mL PbS UC device with 3 mM TCA **(d)** 25 mg/mL PbS UC device with 3 mM TCA **(e)** 50 mg/mL PbS UC device with 3 mM TCA. Threshold intensities (bottom right) and slopes of linear and quadratic regimes are indicated.

Sample	Threshold Intensity (W/cm^2)
5 mg/mL PbS, No TCA	4.50
5 mg/mL PbS, 3 mM TCA	2.82
10 mg/mL PbS, 3 mM TCA	2.05
25 mg/mL PbS, 3 mM TCA	1.87
50 mg/mL PbS, 3 mM TCA	0.996

Table SI 1: Table of measured threshold intensities for UC devices.

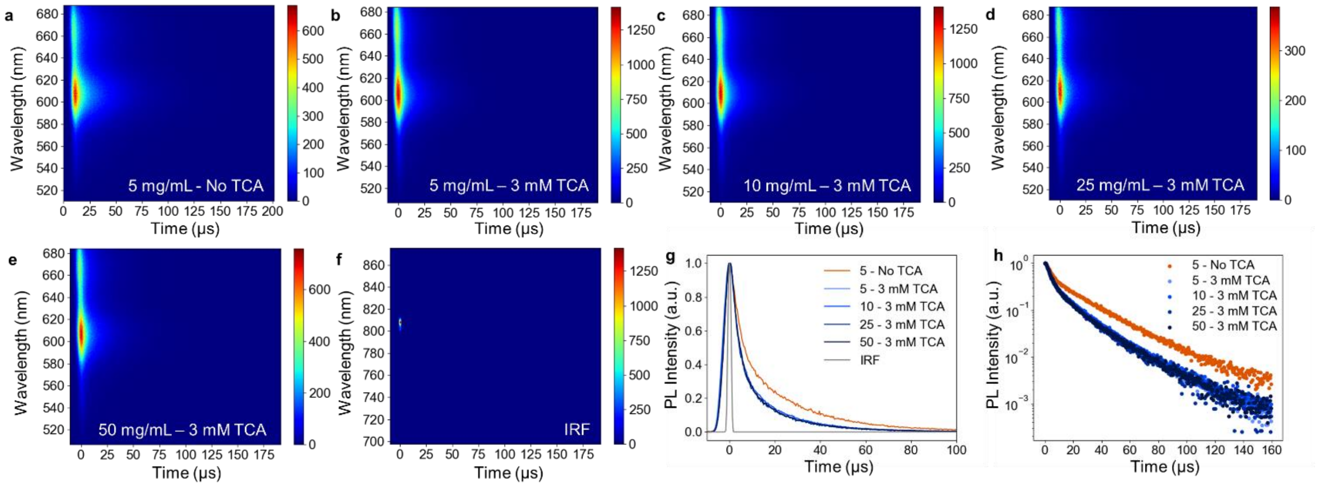

Figure SI 10: Time resolved upconversion photoluminescence decays for upconversion devices with **(a)** 5 mg/mL PbS – no TCA, **(b)** 5 mg/mL PbS – 3 mM TCA, **(c)** 10 mg/mL PbS – 3 mM TCA, **(d)** 25 mg/mL PbS – 3 mM TCA, **(e)** 50 mg/mL PbS – 3 mM TCA **(f)** Instrument response function decay **(g)** Normalized decay curves **(h)** Normalized decay curves on logarithmic scale.

	A_1 (%)	τ_1 (µs)	A_2 (%)	τ_2 (µs)	τ_{avg} (µs)	R^2	Fluence (J/cm^2)
5 mg/mL - No TCA	57.3	4.86	42.7	29.76	15.50	0.997	0.23
5 mg/mL – 3 mM TCA	70.0	4.05	30.0	20.94	9.11	0.998	
10 mg/mL – 3 mM TCA	69.2	4.20	30.8	21.44	9.51	0.998	
25 mg/mL – 3 mM TCA	72.7	4.24	27.3	21.16	8.86	0.994	
50 mg/mL – 3 mM TCA	72.8	4.35	27.2	21.38	8.99	0.997	

Table SI 2: Table of TRUCPL decay fitting constants for 5 mg/mL UC device without TCA, and 5, 10, 25, and 50 mg/mL UC devices with 3 mM TCA.

Figure SI 11: (a, b) Schematic diagram and photograph of the anti-counterfeiting imaging set up with (1) Kiralux 8.9 MP Color CMOS Camera with imaging lens, (2) Imaging lenses, (3) 850 nm LED (M850L3), (4) sample holder for patterned UC device.